1   **Nonlinear inversion of tilt-affected very-long-period records of explosive eruptions at**

2   **Fuego volcano**

3   **Gregory P. Waite[1] and Federica Lanza[1]**

4   [1]Department of Geological and Mining Engineering and Sciences, Michigan Technological

5   University, Houghton MI 49931 USA.

6

7   Corresponding author: Greg Waite (gpwaite@mtu.edu)

8

9

10   **Key Points:**

11   • Near-field seismic recordings of explosions from Fuego volcano include signal well

12   below corner frequencies

13   • Inversion allows for inclusion of tilt affected signal

14   • Nonlinear inversion for source type provides quantitative description of moment tensor

15   uncertainty

16

17   **Abstract**

18   Magmatic processes produce a rich variety of volcano seismic signals, ranging over

19   several orders of magnitude in frequency, and over a wide range of mechanism types. We

20   examined signals from 400-10 s period associated with explosive eruptions at Fuego volcano

21   Guatemala that were recorded over 19 days in 2009 on broadband stations with 30 s and 60 s

22   corner periods. The raw data from the closest stations include tilt effects on the horizontal

23   components but also have significant signal at periods below the instrument corners on the

24   vertical components, where tilt effects should be negligible. We address the problems of tilt-

25   affected horizontal waveforms through a joint waveform inversion of translation and rotation,

26   which allows for an investigation of the varying influence of tilt with period. Using a phase-

27   weighted stack of six similar events, we invert for source moment tensor using multiple bands.

28   We use a grid search for source type and constrained inversions, which provides a quantitative

29   measure of source mechanism reliability. The 30-10 s bandpass results are consistent with

30   previous work that modeled data with a combined two crack or crack and pipe model. At the

31   longest-period band examined, 400-60 s, the source mechanism is like a pipe that could represent

32   the shallowest portion of the conduit. On the other hand, source mechanisms in some bands are

33   unconstrained, presumably due to the combined tilt-dominated and translation-dominated

34   signals, which are not coincident in space and have different time spans.

35   **1 Introduction**

36   Volcanic eruptions produce ground deformation over a broad range of frequencies that

37   are routinely modeled to provide insight into conduit structure, eruption mechanisms, and

38   magma properties. Seismic source inversions use data from a relatively small frequency range

39   but are enlightening especially when interpreted in conjunction with complementary data. Both

40   seismic source inversion and the interpretation of models are individually challenging. In this

41   study, we address aspects of both of these challenges by using a nonlinear inversion approach for

42   combined ground translation and rotation data recorded at Fuego volcano, Guatemala.

43   Seismic waves are sensitive to ever smaller-scale heterogeneities with increasing

44   frequency, meaning models of Earth elastic properties must be sufficiently detailed for modeling

45   propagation effects. At most volcanoes the velocity structure is poorly known so that path and

46   source affects cannot be separated for the most energetic frequencies (0.5 – 5 Hz or so). One

2

47 solution to this is to evaluate long wavelength, very-long-period (VLP) data that are relatively

48 insensitive to unmodeled heterogeneity. The VLP band, commonly defined to be between 2 and

49 100 s period, is associated with wavelengths from 10s to 100s of km. At epicentral distances of a

50 few km, the only important path effect is related to surface topography. The relative ease of

51 modeling the path has allowed for investigation of VLP source mechanisms at volcanoes

52 throughout the world [*Chouet and Matoza*, 2013; *Waite*, 2015].

53 However, an additional complication arises when recordings are made in the near field,

54 especially for shallow sources. While ground rotation (tilt) has little effect on the vertical

55 component of the seismometer, horizontal components are sensitive to rotation through

56 gravitational acceleration [*Rogers*, 1968]. The apparent displacement can dominate at periods

57 below the instrument corner (typically between 30 and 120 seconds for a broadband

58 seismometer), so that tilt signals with periods in the VLP band can have significant apparent

59 displacement. This is particularly problematic when displacement at periods below the

60 instrument corner is evident.

61 Fortunately, just as the instrument response to translation can be accurately modeled, so

62 too can the response to ground tilt [*Aoyama and Oshima*, 2008; *Lyons et al.*, 2012]. *Maeda et al.*

63 [2011] proposed a method for jointly inverting for ground translation and rotation. In this

64 approach, separate Green's functions for ground rotation and translation are computed and

65 convolved with the appropriate rotation or translation instrument responses prior to inversion.

66 The raw, bandpass filtered seismograms are effectively deconvolved during the inversion.

67 Moment tensors are equivalent force systems and as such do not strictly represent the

68 model for a seismic event. Tensors are commonly decomposed into two or more geologically

69 reasonable tensors that model the physical source process. While this approach is appropriate, it

70 involves somewhat arbitrary choices about contributing mechanisms. We address the challenge

71 of determining a physical model for the moment tensor source time functions through a nonlinear

72 inversion for source types. This approach allows for quantification of the importance of Double-

73 Couple (DC), or Compensated Linear Vector Dipole (CLVD) versus volumetric components.

74 We use a constrained inversion and search over all possible source types and orientations to

75 compare model fits for all possible source types.

76   Fuego is a 3800 m stratovolcano that regularly produces Strombolian and weak

77   Vulcanian explosions. The dynamics of these explosive events have been examined in the VLP

78   band [*Lyons and Waite*, 2011] and modeled together with infrasound and gas emission data. At

79   least three different styles of VLP event have been observed and attributed to eruptions from

80   either the summit vent or a flank vent [*Waite et al.*, 2013]. The strongest recorded explosions

81   generated impulsive infrasound and seismic signals, ejected incandescent bombs and tephra, and

82   were associated with repetitive VLP seismicity. The previous studies of Fuego VLP events

83   focused on periods from 30-10 seconds, where the influence of ground tilt is negligible given the

84   distances to the source and relatively short VLP wavelengths. Although the station geometry was

85   somewhat limited by the logistical and safety considerations, *Lyons and Waite* [2011] found that

86   the data best fit a source with a centroid 300 m below and 300 m to the west of the summit with a

87   moment tensor representative of primarily a dipping crack. The 30-10 second VLP captures the

88   inflation-deflation-reinflation cycle of this portion of the conduit as a small eruption occurs.

89   *Lyons et al.* [2012] examined the tilt signal associated with these same small explosions

90   at periods below the instrument corners. They found a significant tilt signal beginning up to 30

91   minutes prior to explosive eruptions. Forward modeling of the tilt from stations that were close

92   enough to record it suggested a shallow source midway between the VLP source centroid and the

93   summit. A full waveform inversion was not attempted.

94   In this study, we perform full waveform inversions of stacks of events associated with

95   summit vent explosions in periods from 400 - 10 seconds using a combined rotation-translation

96   approach similar to that of *Maeda et al*. [2011]. Inversions were performed in different bands to

97   explore the increasing influence of tilt with increasing period. While events with periods of 100s

98   of seconds are sometimes called Ultra-Long-Period events [e.g., *Johnson et al.*, 2009], we simply

99   use the term VLP to cover the range of periods we investigate here. To improve the signal to

100   noise ratio, and ensure a representative dataset, inversions were performed on a set of phase-

101   weighted, stacked seismograms from six explosions. The cleaner signals that resulted from

102   stacking also allowed for a larger number of seismic channels to be used than in previous studies.

103   In order to constrain the uncertainty on the source type, we performed a nonlinear inversion for

104   moment tensor source type. This involves a grid search over all possible moment tensor types

105   and orientations at the best-fit centroid location, providing quantitative constraint on the source

106   type.

107   **2 Inversion methodology**

108   2.1 Joint rotation and translation inversion

109   In order to avoid problems associated with ground rotation contaminating the low

110   frequency seismic signal and, in fact, to take advantage of the tilt signal to investigate

111   frequencies below the typical VLP band, we invert jointly for translation and rotation. The

112   approach was first laid out by *Maeda et al*. [2011] and has been successfully applied at Kīlauea

113   [*Chouet and Dawson*, 2013] and Asama volcanoes[*Maeda and Takeo*, 2011] . An important

114   aspect of this method is that the instrument responses are not deconvolved from the

115   seismograms. Instead, the responses to tilt and displacement are convolved with corresponding

116   Green's functions. Deconvolution effectively occurs during the inversion. For component *n* of

117   displacement at time *t* and receiver position $\vec{r}$, we can write the relationship between source and

118   receiver through rotation and translation Green's functions in the frequency domain:

$$u_n^{seis}(\vec{r},\omega) = \left[I_n^{rot}(\omega) G_{np,q}^{rot}(\vec{r},\omega) + I_n^{trans}(\omega) G_{np,q}^{trans}(\vec{r},\omega) \right] M_{pq}(\omega), \tag{1}$$

120   where $u_n^{seis}(\vec{r},\omega)$ is the Fourier transform of the *n* component of the seismogram without

121   instrument correction, *p* and *q* are direction indices *x*, *y*, and *z*, $M_{pq}(\omega)$ is the Fourier transform

122   of the time history of the *pq*-component of the moment tensor, I^{rot} and I^{trans} represent tilt and

123   translation instrument response functions, the matrices G^{rot} and G^{trans} are Green's functions that

124   relate the *n*-component of tilt or translation at the receiver position, $\vec{r}$, with the moment at the

125   source position, and ω is angular frequency. The notation *p,q* indicates spatial differentiation

126   with respect to the *q*-coordinate. The translation response is derived from the poles and zeros in a

127   standard way, while the tilt response is defined as $I^{rot} = g\, I^{trans}\, (i\omega)^{-2}$ [*Maeda et al*., 2011], where

128   *g* is gravitational acceleration. We assume no tilt response on the vertical components. Although

129   it is not specified in equation (1), the *G* matrices naturally depend on the source position as well.

130   In practice, we do not invert directly for the source position, instead searching over a volume of

131   possible source locations and determining the source position from the inversion results.

132   Equation 1 can be recast in matrix form as

$$\mathbf{u}(\omega) = \mathbf{G}(\omega)\mathbf{s}(\omega), \tag{2}$$

134   where **u** is the *R* x 1 vector of Fourier-transformed ground displacement components, **s** is the 6 x

135   1 vector of Fourier transformed moment-tensor components to be determined, and *R* is the

136   number of observed seismic traces. The matrix **G** is *R* x 6, composed from Fourier transform of

137   the terms inside the square brackets in equation 1. The equation is solved in a least-squares

138   inversion one frequency at a time, as described in *Waite et al.* [2008]. Initially, the inversion is

139   unconstrained, and the model moment tensor source time function is constructed from the

140   inverse Fourier transform of the inversion results. Although some studies have found that single

141   forces can be important in VLP source processes, especially when related to a reaction to vertical

142   mass ejection, previous work at Fuego [*Lyons and Waite*, 2011] showed they were not

143   significant. Single forces are unlikely to contribute to even lower frequency source models,

144   which are dominated by pre-explosion signal, so they were not considered in our study.

145   2.2 Green's functions

146   The translation and rotation Green's functions were calculated using a finite-difference

147   method [*Ohminato and Chouet*, 1997] with a homogeneous model that includes the three-

148   dimensional topography of Fuego volcano. Given the long wavelengths of the VLP signals, the

149   homogeneous structure is appropriate [see, e.g., *Waite et al.*, 2008]. We used a compressional-

150   wave velocity of 3.5 km/s, shear-wave velocity of 2 km/s, and density of 2650 kg/m^3. In practice,

151   the error in the velocity model introduces little effect on the VLP inversion [*Waite et al.*, 2008].

152   The model is centered on the summit of Fuego and extends 11.72 km east-west, 8.96 km north-

153   south, and 6 km vertically with a 40 m grid spacing. Green's functions for synthetic sources over

154   a volume 680 m east-west, 480 m north-south, and 920 m vertically from the summit down. This

155   volume is centered west of the summit, because the VLP source found by *Lyons and Waite*

156   [2011] was ~300 m west of the summit vent. In order to speed the calculations, we skip

157   alternating grid nodes, so the synthetic source volume has a spacing of 80 m. All other details

158   about the finite-difference modeling are as described in *Lyons and Waite* [2011]. The rotation

159   Green's functions are computed from the curl of the displacement field (two times the tilt) during

160   the finite-difference simulations.

161   2.3 Nonlinear inversion procedure

162   The unconstrained inversion at hundreds of points inside a volume within the summit of

163   Fuego volcano provides a spatial estimate of the location and uncertainty on the location (see

164   section below). Interpretation of the moment tensor source time function can be done by point-

165   by-point eigenvector decomposition, which provides the orientation and mechanism type in cases

166   where the moment components are in phase throughout the source time function. We expand on

167   this approach to explore the uncertainty in the moment tensor type, following the nonlinear

168   inversion approach described below.

169   Our approach involves a grid search over a total of five parameters for all possible

170   moment tensor types and orientations. For each model, we constrain the moment tensor using the

171   method of Lagrange multipliers and compute the data fit. First, we search over possible moment

172   tensor types using the fundamental lune source-type definition of *Tape and Tape* [2012], which

173   involves two parameters that describe the ratios of the moment tensor eigenvalues (Figure 1).

174   The latitude parameter, δ, ranges from $-90°$ to $90°$ and the longitude parameter, γ, ranges from $-$

175    $30°$ to $30°$. Some example source types, the associated γ and δ, along with relative eigenvalues

176   (λ) are given in Table 1 and in Figure 1. We refer readers to *Tape and Tape* [2012] for a

177   thorough description of the lune parameterization.

178   **Table 1.** Relationship between moment tensor eigenvalues, lune latitude and lune longitude

	γ	δ	λ_1	λ_2	λ_3
Isotropic $(+\Delta V)^a$		90°	1	1	1
DC	0°	0°	1	0	-1
CLVD[b]	-30°	0	2	-1	-1
Crack ($v=1/4, +\Delta V$)[a]	-30°	60.50°	3	1	1
Crack ($v=1/3, +\Delta V$)[a]	-30°	70.53°	2	1	1
Pipe ($v=1/4, +\Delta V$)[a]	30°	74.21°	2	2	1
Pipe ($v=1/3, +\Delta V$)[a]	30°	79.98°	1.5	1.5	1

179   [a]only positive δ (volume increase) examples are shown

180   [b]only the left CLVD is shown

181   Examples for two different Poisson ratios are shown for the crack and pipe models.

182

183   The search over the parameters γ and δ uses the surface spline method described by *Tape*

184   *and Tape* [2012] to evenly sample the moment tensor source type space. This method results in a

185   substantial computational savings over an evenly sampled grid [*Wang and Dahlen*, 1995]. We

186   evaluate γ from $-30°$ to $30°$, but because the lower half of the lune is simply the opposite sign of

187   the upper half (e.g., volume decrease versus volume increase), we evaluate δ from 0 to $90°$.

188   To explore the full moment tensor space requires modeling the range of possible

189   orientations. We rotate the moment tensor at 10º intervals using a sequence of three rotations

190   about the initial coordinate system of the moment tensor. Full sampling of the symmetric tensor

191   involves a 360º range about the *z* axis, 180º of dip, and 90º of rotation about the new, rotated *z'*

192   axis [*Goldstein et al.*, 2001]. Tests with finer intervals showed little difference in the pattern of

193   misfits on the lune and minor variation in the misfit values. This involves 5832 combinations of

194   rotation angles combined with 223 γ - δ pairs.

195   For each of the 1,300,536 trial moment tensor solutions, the six independent moment

196   tensor components of the trial tensor are used to constrain the inversion through a system of

197   equations, that fix the ratio of the moment tensor components [*Menke*, 1989]. For a given trial

198   tensor, **H** is a matrix that contains the ratios of matrix components to arbitrarily selected

199   component $M_{11}^{(n)}$:

200

$$
\mathbf{H} = \begin{bmatrix}
1 & -M_{11}^{(n)}/M_{22}^{(n)} & 0 & 0 & 0 & 0 \\
1 & 0 & -M_{11}^{(n)}/M_{33}^{(n)} & 0 & 0 & 0 \\
1 & 0 & 0 & -M_{11}^{(n)}/M_{12}^{(n)} & 0 & 0 \\
1 & 0 & 0 & 0 & -M_{11}^{(n)}/M_{23}^{(n)} & 0 \\
1 & 0 & 0 & 0 & 0 & -M_{11}^{(n)}/M_{13}^{(n)}
\end{bmatrix}
$$

201   where the notation $M_{11}^{(n)}$ indicates the *n*th trial moment tensor. The constraint equations are

202   solved simultaneously in the inversion using least squares:

203

$$
\begin{bmatrix} \mathbf{G^T G} & \mathbf{H^T} \\ \mathbf{H} & \mathbf{Z} \end{bmatrix} \begin{bmatrix} \mathbf{s} \\ \mathbf{l} \end{bmatrix} = \begin{bmatrix} \mathbf{G^T u} \\ \mathbf{h} \end{bmatrix}
$$

204   where **Z** is a 5 x 5 matrix of zeros, **h** is a 5 x 1 vector of zeros, and **s** and **u** are the model and

205   data vectors as in equation 2. The vector **l** consists of the Lagrange multipliers.

206   Given the large number of possible solutions, we perform the full grid search for only the

207   best-fit locations of each frequency band. Given that the source time function does not vary

208   rapidly spatially [*Lyons and Waite*, 2011], this is a reasonable approach.

209   2.4 Error analysis

210   The nonlinear approaches to finding the best centroid location and moment tensor lend

211   themselves to quantitative error analysis. Misfit information is used to define uncertainty on the

212   source centroid, and in this work we extend this to examine uncertainty in the moment tensor

213   type. A similar approach was used by *Ford et al.* [2010] to examine non-double-couple

214   components of explosion and earthquake sources. In many applications of moment tensor

215   inversion at volcanoes, a weighted squared error is used, which is either normalized by station or

216   channel [*Chouet et al.*, 2003; *Ohminato et al.*, 1998]. As our approach follows this methodology,

217   we adopt the squared error measure described as E_2 :

218
$$E_2 = \frac{1}{N_r}\sum_{n=1}^{N_r}\left[\frac{\sum_1^3\sum_{p=1}^{N_s}\left(u_n^0(p\Delta t)-u_n^s(p\Delta t)\right)^2}{\sum_1^3\sum_{p=1}^{N_s}\left(u_n^0(p\Delta t)\right)^2}\right] \tag{3}$$

219   where $u_n^0(p\Delta t)$ is the *p*th sample of the *n*th data trace, $u_n^s(p\Delta t)$ is the *p*th sample of the *n*th

220   synthetic trace, N_s is the number of samples in each trace, and N_r is the number of three-

221   component receivers. Here the squared error is normalized by station, so that stations with

222   varying amplitude contribute equally to the error.

3 Seismic data

3.1 Temporary seismic network

225   Our seismic data were recorded on a network of 10 three-component broadband

226   seismometers from 8-26 January 2009, 8 of which are shown in Figure 2. The network

227   configuration was limited by the steep topography, deep ravines, thick jungle, and safety

228   considerations due to the eruptive activity. Six of the sites were equipped with Güralp CMG 40T

229   sensors (0.02– 30 s) and four sites featured Güralp 3 ESPC sensors (0.02– 60 s). Data were

230   recorded on 10 Reftek 130 digitizers operating in continuous mode at 100 samples per second.

231   The threat of vandalism or theft prohibited deployment of solar panels at some sites, so

232   continuous operation of all 10 stations was restricted to 19 - 21 January. Two of the stations are

233   very close to F9A, F9B, and F9C, and were not used in the study. Station F9SE, at 6 km from the

234   summit, did not record the VLP signals. In total, seven stations (21 channels) were used in the

235   inversions. More complete details of the experiment are given in *Lyons and Waite* [2011].

236   3.2 VLP events

237   During this deployment, all of the strong explosions issued from the summit vent and

238   produced clear VLP signals at the nearest stations. The closest station, which also happened to be

239   the most reliable, F900, recorded hundreds of similar explosions during the 19-day deployment.

240   *Lyons and Waite* [2011] selected one of these events (19 January 2009 at 16:09:30) that was well

241   recorded on the network for their inversion. In order to improve the signal-to-noise ratio of the

242   data on some of the more distant channels, especially at periods below 30 seconds, we computed

243   phase-weighted stacks of similar events in multiple frequency bands for inversion.

244   The 19 January event was used as a master event and compared against all the data at

245   station F900. With this procedure, we identified 209 events for which the combined three-

246   channel cross-correlation coefficient was 2.0 or greater (roughly one event every 2 hours). Of

247   these, only 21 events were simultaneously recorded on all the stations from 19-21 January. The

248   waveform similarity generally degraded with increased distance from the source. While the

249   waveforms were generally consistent from event to event on a given channel in the 30-10 second

250   band, and produced a clean stack, the weaker signals and possibly greater noise at lower

251   frequencies led to poor correlations on many channels below 30 seconds. As an objective of this

252   study was to investigate frequencies below the instrument corner, we sought to use only events

253   that were similar. We visually inspected all the data channel-by-channel, and removed all data

254   from events where one or more channels was extremely noisy or had inverted polarity in the 400

255   to 60 or 60 to 10 seconds band. This left just six events to stack for the inversion.

256   We followed the phase-weighted stacking approach of *Schimmel and Paulssen* [1997]

257   and found that it produced a vastly improved signal to noise ratio (Figure 3). This is particularly

258   important for the lower frequencies, which contain substantially more noise on a single trace.

259   Even with just six events in the stack, the phase-weighted stacking procedure resulted in clean

260   waveforms at nearly every channel and every station. For comparison, we show the linear stack

261   along with the individual waveforms from all the events for the vertical component at three

262   stations in two non-overlapping frequency bands. In general, the phase-weighted stack is slightly

263   lower in amplitude but has much less pre- or post-event noise. In particular, single-event noise

264   that contributes substantially to the linear stack is absent in the phase-weighted stack.

265   The gray bars in Figure 3 mark the range of arrival times for the peak infrasound

266   associated with each of the six explosions. The infrasound sensor was collocated with station

267   F900 at distance of approximately 800 m from the vent, so the travel time is negligible at the

268   scale of the figure. Interestingly, the range of infrasound arrival times is nearly 4 seconds relative

269   to the waveform correlation of VLP signals at F900.

270   Figure 3 also highlights the difference between the vertical components in the low-

271   frequency band. We expect no tilt on the vertical components, yet the events are evident in the

272   400-60 s band, especially on the 60 s stations (F9NW, F9B, F9SW, F9NE). This suggests that

273   the events produce translational motion at frequencies below the instrument corner. Figure 4,

274   which shows the spectra for each of the bands analyzed at three stations, further highlights the

275   vertical component signal well below the instrument corner. The spectra also demonstrate the

276   large amplitude of the horizontal components at the lowest frequencies. Given the known

277   influence of tilt on the horizontal components at those low frequencies, a joint inversion

278   approach is required to investigate frequencies below the corner of the sensors. Only station

279   F9SE, which was ~6 km from the vent, did not record signal in the VLP band, so it was omitted

280   from further analysis.

281   **4 Inversion results**

282   The presence of significant vertical-component signal on records filtered below the

283   corner frequencies of the sensors implies that these explosion events produced measureable

284   translation component at those low frequencies. Because the influence of tilt increases with

285   lower frequency, just as the sensitivity to translation decreases, we evaluated the VLP data

286   source mechanisms in several overlapping bands between 10 and 400 seconds period. For each

287   bandpass, we first found the best-fitting solution by searching over the range of locations

288   described above. At each position, we inverted for the moment-tensor solution that best fit the

289   data without constraining the solution in any way. Because no constraints are used in the

290   inversion, there is the possibility for model source time functions to be inconsistent over time,

291   resulting in an uninterpretable, geologically unreasonable model. Therefore we used a second

292   step that measures the stability of the moment tensor throughout the source time function to

293   identify the best solution for each bandpass.

294   In this second step, we evaluated consistency of the source time function over its duration

295   using a statistical measure. This statistic, which was called gamma by *Matoza et al.* [2015], we

296   call g to avoid confusion with the previously defined moment-tensor lune longitude. For each

297   point in the source time function, we compute the eigenvalues. If the maximum eigenvalue is

298   within 60% of the peak value, we then compute the ratios of the intermediate to maximum, IM,

299   and minimum to maximum, mM, eigenvalues. Restricting the analysis to only the large

300   amplitudes ensures that the statistic reflects the main features of the source time function. We

301   then compute the standard deviations of the sets of ratios of the eigenvalues. These standard

302   deviations provide a measure of the consistency of the source time function. They may be more

303   useful if we use them to compare the source time function with a predetermined model. To do

304   this, we multiply each of the ratios by the maximum to intermediate or maximum to minimum

305   ratio for a known source prior to computing the standard deviations. For example, comparing the

306   source time function to a crack with ratios of 2:1 and 2:1 would mean multiplying each of the

307   ratios by 2, then computing the standard deviations. The standard deviations are then combined

308   into one value using the square root of the sum of the squared standard deviations. Since *Lyons*

309   *and Waite* [2011] found the 30-10 second period VLP source to be dominated by a dipping

310   crack, we used moment tensor eigenvalue ratios of 2:1:1. We also examined g for ratios of 3:1:1

311   and 1:1:1 and, although the values for g varied, we found no difference in which of the solutions

312   had the lowest g. Because it implies the most consistency throughout the source time function,

313   the solution within 5% of the minimum E_2 error that had the lowest g was chosen as the best

314   solution.

315   4.1. Free inversion results

316   The best-fit centroid locations do not vary significantly with bandpass. The minimum E_2

317   solutions (E_{2min}) are identical for bands from 60-10 s through 400-10 s, all very near the surface

318   and just west of the summit (see Figure 5 and Table 2). When the minimum g is also considered,

319   the best solutions are deeper, and the 60-10 s and 90-10 s solutions are 320 m east of the summit.

320   The 120-10 s and 400-10 s solutions are about 80 m south of the E_{2min} solutions. The lowest

321   frequency (400-60 s) g_{min} solution is at a shallower depth and location nearer the summit than the

322   E_{2min} solution. The best 30-10 s solutions are west of the summit when both E_{2min} and g_{min} are

323   considered; it only migrates south to north. The E_{2min} solution is within 200 m of the best fit

324   found by *Lyons and Waite* [2011] when inverting in the same 30-10 s band, although we use a

325   stack of 6 events that allows us to invert data from an additional station. We do not attempt to

326   interpret the fine details of the centroid locations, given the limitations in the station coverage,

327   but consider the locations to be geologically reasonable.

328   Given the similarities in models for some of the intermediate bandpasses, we focus on

329   four representative bands: 30-10 s; 90-10 s; 120-10 s; and 400-60 s. The E_{2min} and g_{min} centroid

330   locations are shown in Figure 5. In Table 2, the E_{2min} and g_{min} solutions for each bandpass are

331   shown, with the E_{2min} in the first row and g_{min} in the second row.

332   Figure 6 shows data (black) and synthetic waveforms for each of the four bandpasses.

333   The free inversion synthetics, shown in red, generally fit the data quite well. The error measure

334   we use weights stations, not channels, equally. The advantage to this is that stations that are

335   farther away or have lower amplitude because of the radiation pattern have equal importance. To

336   give a sense of the fits on individual channels, we computed cross-correlation coefficients and

337   lag times between the data and free inversion synthetics. At F900, for example, the fits at all

338   channels in the 30-10 s bandpass are above 0.97 at lags of between -0.04 and 0.28 s. In contrast,

339   the north channel at F9A, which clearly fits less well, has a correlation coefficient of 0.83 at 0.02

340   s lag. The worst-fitting channel, the east channel of F9NW, has a correlation of 0.53 at 6.5 s lag.

341   More than half of the correlation coefficients are above 0.9 in the 90-10 s band, and none of the

342   lags are more than 1 s. In each of the remaining two bands, at least 5 channels correlate above

343   0.9. The range of lag times increases slightly in the longer period bands but, even in the 400-60 s

344   band, well over half of the lags are below 5 sec.

345   The synthetics from the fixed tensor solutions, described below, have slightly greater

346   misfits, as expected for models with fewer free parameters. The synthetics for the 90-10 s band

347   are notably much poorer for the fixed inversion. The correlation coefficients and lag times

348   between the data and both the free inversions and the fixed tensor inversions for each of the

349   channels are given in supplementary tables S1 and S2, respectively.

350   The source time functions for these same four representative bandpasses are shown in

351   Figure 7. They share some common features, with the dipole components in phase, and apart

352   from the 90-10 s band, dominating the source time function. There are differences in the

353   eigenvectors and eigenvalues, although the major difference is between the 90-10 s band and the

354   others. The median ratios of minimum and intermediate eigenvalues to the largest are shown in

355   Table 2. The source types are described in the next section.

356

357   **Table 2.** Best solution information as a function of bandpass

Bandpass (seconds period)	E-W position relative to summit [m]	N-S position relative to summit [m]	Depth below the summit [m]	E_2	g	Eigenvalue ratios
30-10[†]	280 W	0	280	0.177		
30-10	360 W	80 S	120	0.288	0.088	
	280 W	160 N	120	0.316	0.068	1, 0.28, 0.12
90-10	200 W	0	40	0.418	0.221	
	120 E	0	120	0.441	0.156	1, 0.09, -0.28
120-10	200 W	0	40	0.425	0.222	
	200 W	80 S	200	0.465	0.193	1, 0.73, 0.30
400-60	360 W	160 N	360	0.396	0.337	
	200 W	80 S	200	0.427	0.105	1, 0.78, 0.21

358   [†] solution of *Lyons and Waite* [2011] is shown for comparison. In that study, error was computed

359   for 17 channels, compared with 19 channels used in this study, which led to much larger misfits.

360   For the remaining rows, the first row associated with each band represents details of the E_{2min}

361   solution and the second row shows details of the g_{min} solution.

362

4.2. Constrained inversion results

364   For each of the representative bandpasses, the centroid location with the lowest g that

365   was also within 5% of E_{2min} was used to investigate the constraint on the source type. The

366   nonlinear analysis demonstrates that the range of models with similar misfits is fairly broad.

367   Figure 8 shows the misfits at each moment tensor type for the lowest misfit tensor orientation.

368   The point-by-point source time function eigenvalue analysis for the best free inversion is shown

369   using red dots. These correspond to the γ and δ at each point in the source time function when

370   the amplitude was within 50% of the maximum. Points with negative δ were projected to the

371   upper portion of the plot. The misfits for the constrained inversion results are much larger than

372   those of the free inversions, because the moment tensor is fixed for the whole source time

373   function. This means there is essentially one model parameter in the constrained inversions,

374   compared to six independent model parameters for the free inversions. Each point in this lune

375   plot represents the lowest misfit value for all moment-tensor orientations with the γ - δ pair.

376   Considering, first, the solution in the 30-10 s band, the minimum misfit in the constrained

377   inversions is 0.43, compared to 0.32 for the g_{min} solution. The point-by-point γ–δ pairs are tightly

378   constrained, and the median ratio of eigenvalues is (1.0, 0.28, 0.12). But the nonlinear inversion

379   for source type suggests a wider range of possible mechanism types fit the data. In Figure 8a, the

380   0.46 misfit contour encompasses the points in the free inversion and is about 5% above the

381   minimum, and so might be considered a reasonable level to explore the range of possible models.

382   This includes sources from a tension crack to a DC.

383   One interpretation of this is that the source represents a composite of two or more sources

384   that have different orientations. In fact, *Lyons and Waite* [2011] found that a combination of a

385   single dipping crack and nearly vertical pipe or crack provided the best-fitting model for the 30-

386   10 s VLP. The two sources were out of phase and interpreted to represent the opposite sense of

387   volume change. That is, when the vertical dike or pipe was deflating, the dipping sill was

388   inflating. We computed the γ - δ pair for the combined crack-pipe tensor of *Lyons and Waite*

389   [2011], which is dominated by the crack, and plotted it in Figure 8a. This combined mechanism

390   is actually closer to a single crack than the free inversion solution, with γ=-22 and δ=58. The

391   two-crack model of *Lyons and Waite* [2011] is in a similar location (γ=-20 and δ=63). The

392   relatively small range of E_{2min} values, compared to Figure 8c and d, throughout the lune space

393   indicates multiple source types can fit the data well.

394   As is clear from Figure 8b, the 90-10 s bandpass data do not constrain the source type.

395   Clearly, even the g_{min} solution is much less stable than the 30-10 s solution, and this is born out

396   in the nonlinear inversion for source type. Very little can be interpreted from this solution, but

397   note that the median eigenvalue ratios include a negative minimum and the point-by-point γ -

398   δ pairs are all below the region in which all the components have the same sign. The poorly

399   constrained solution is probably mainly due to the complexity of the source. On some stations,

400   especially in the horizontal components, the spectra show two peaks between 90 and 10 s period,

401   which we might infer are tilt dominated, and translation dominated. These may reflect two

402   sources, distinct in space and with peak moment release occurring at distinct times.

403   At the wider 120-10 s bandpass, the lower frequencies tend to dominate and the nonlinear

404   inversion for source type is somewhat better constrained. The free inversion is better constrained

405   than the 90-10 s band, but the point-by-point γ - δ pairs still range widely. In this case, however,

406   the points are all in the region of a volumetric source. The median ratio of eigenvalues is (1.0,

407   0.73, 0.30) the nonlinear inversion (Figure 8c) points to a source somewhat like a pipe.

408   The final example we present is the 400-60 s band, below the corners of any of the

409   sensors. This inversion is much better constrained in both the free inversion and constrained

410   nonlinear inversion. The γ - δ pairs from the free g_{min} inversion cluster near the point defined for

411   a pipe (1.5, 1.5, 1) and the median eigenvalues are (1.0, 0.78, 0.21). The range of misfit values is

412   much larger than in the previous inversions, and the region surrounding 5% above the minimum

413   occupies a relatively small area. In this case, the source type is well constrained to a volumetric

414   source, and eigenvalues suggest a mechanism like a pipe. Based on the eigenvectors a pipe

415   would be dipping about 30º to the NNE, which is reasonable given the centroid location.

416   **5 Discussion**

417   These results do not necessarily simplify the interpretation of these events, but the

418   nonlinear inversion for source type provides a better means of assessing the reliability of the

419   models. In some cases, like the 400-60 s band result, the model is tightly constrained and can be

420   interpreted in terms of a portion of the conduit just below the vent that inflates and deflates

421   during each explosion. In other cases, such as the 30-10 s band, the nonlinear inversion results

422   suggest that a range of solutions from double-couple to a tension crack can explain the data

423   equally well. This can also be seen as evidence for a complex source that involves two or more

424   sources acting more-or-less coincidentally, but with opposite phase. Finally, the 90-10 s band is

425   an example that cannot be constrained to a model. In this case, we suggest that it is because it

426   includes both the crack-like source of the 30-10 s band west of the summit and the pipe-like

427   source of the 400-60 s band closer to the summit.

428   Our interpretation is consistent with earlier work at Fuego, and we refer to *Lyons and*

429   *Waite* [2011] for detailed discussion of the source dynamics of the VLP events. Apart from the

430   quantitative description of the source-type uncertainty, the key new results involve the formal

431   moment-tensor solutions for periods below 30 s. The results of inversion for tilt-affected and tilt-

432   dominated signals are consistent with forward modeling by *Lyons et al*. [2012] of tilt derived

433   from four broadband stations to the north of the summit. In their study, they found that tilt

434   signals could be described by a spherical source just below the summit. While our inversions

435 suggest a source somewhat more like a dipping pipe than a pure sphere, the location and sense of

436 volume change are consistent.

437   The tilt-dominated signal begins with inflation several minutes prior to the explosion

438 (Figure 7d). Although we limited the band to 400 seconds, a much longer lead-up time can be

439 seen in the raw data when integrated [*Lyons et al.*, 2012]. This is interpreted as pressurization

440 following sealing of the conduit in the summit area. The model for the 30-10 s VLP proposed by

441 *Lyons and Waite* [2011] has pre-explosion inflation, mainly in a dipping sill, followed by

442 deflation of that portion of the conduit during the eruption. Our single model moment tensor

443 inversions are consistent with this and we favor this interpretation.

6 Conclusions

445   Volcanic seismic events offer great complexity given the wide range of frequencies,

446 influence of near-field effects including ground rotation, and wide range of source types. We

447 adapt a moment-tensor inversion methodology for including tilt-affected seismograms so that we

448 can examine explosion signals over a range from 400-10 s period, well below the corner periods

449 of the instruments used. These data clearly include translation below the instrument corner, as

450 seen in the vertical components, but likely also include some tilt signal near the instrument

451 corner frequency. We show how a nonlinear inversion for source type can aid in interpretation of

452 the mechanism. In some of the intermediate ranges, the contributions from the longer period,

453 presumably tilt-affected signals and those of the translation dominated signals, mean that a single

454 moment-tensor source cannot fit the data. In other pass bands where either the translation or tilt-

455 affected data dominate, the moment-tensor source types are better constrained.

456   The broadening of the inversion to periods greater than 6 minutes allows for a more

457 complete description of the source. In this case, we find a result that is largely consistent with the

458 forward modeling done in prior work, but offers more detail about the mechanism type. Our

459 interpretation is that the shorter period signals reflect deformation in a shallow crack-like

460 component of the conduit below and west of the summit. The longer periods are due to a

461 shallower component of the conduit just below the summit. Broadband recordings of small-scale

462 explosions are common, and the method we propose could lead to a much better understanding

463 of the shallow dynamics in volcanic conduits in general. Finally, while the explosion events we

464 studied are not particularly hazardous beyond a few hundred meters from the source, they are

465 very common at volcanoes worldwide. An understanding of precursory tilt signals could lead to

466 local warnings of explosions, giving scientists or tourists time to evacuate.

467

475 **References**

476 Aoyama, H., and H. Oshima (2008), Tilt change recorded by broadband seismometer prior to
477   small phreatic explosion of Meakan-dake volcano, Hokkaido, Japan, *Geophys. Res. Lett.*,
478   *35*(6), doi:10.1029/2007gl032988.
479 Chouet, B., and P. Dawson (2013), Very long period conduit oscillations induced by rockfalls at
480   Kilauea Volcano, Hawaii, *J. Geophys. Res.*, *118*(10), 5352-5371, doi:10.1002/jgrb.50376.
481 Chouet, B., P. Dawson, T. Ohminato, M. Martini, G. Saccorotti, F. Giudicepietro, G. De Luca,
482   G. Milana, and R. Scarpa (2003), Source mechanisms of explosions at Stromboli Volcano,
483   Italy, determined from moment-tensor inversions of very-long-period data, *J. Geophys.*
484   *Res.*, *108*(B1), 2019, doi:10.1029/2002JB001919.
485 Chouet, B., and R. S. Matoza (2013), A multi-decadal view of seismic methods for detecting
486   precursors of magma movement and eruption, *J. Volcanol. Geotherm. Res.*, *252*, 108-175,
487   doi:10.1016/j.jvolgeores.2012.11.013.
488 Ford, S. R., D. S. Dreger, and W. R. Walter (2010), Network Sensitivity Solutions for Regional
489   Moment-Tensor Inversions, *Bull. Seism. Soc. Am.*, *100*(5A), 1962-1970,
490   doi:10.1785/0120090140.
491 Goldstein, H., C. P. J. Poole, and L. L. Safko (2001), *Classical Mechanics*, 3rd ed., Pearson.
492 Lyons, J. J., and G. P. Waite (2011), Dynamics of explosive volcanism at Fuego volcano imaged
493   with very long period seismicity, *J. Geophys. Res.*, *116*(B9), doi:10.1029/2011jb008521.
494 Lyons, J. J., G. P. Waite, M. Ichihara, and J. M. Lees (2012), Tilt prior to explosions and the
495   effect of topography on ultra-long-period seismic records at Fuego volcano, Guatemala,
496   *Geophys. Res. Lett.*, *39*, L08305, doi:10.1029/2012GL051184.
497 Maeda, Y., and M. Takeo (2011), Very-long-period pulses at Asama volcano, central Japan,
498   inferred from dense seismic observations, *Geophys. J. Int.*, *185*(1), 265-282,
499   doi:10.1111/j.1365-246X.2011.04938.x.
500 Maeda, Y., M. Takeo, and T. Ohminato (2011), A waveform inversion including tilt: method and
501   simple tests, *Geophys. J. Int.*, *184*(2), 907-918, doi:10.1111/j.1365-246X.2010.04892.x.

502 Matoza, R. S., B. A. Chouet, P. B. Dawson, P. M. Shearer, M. M. Haney, G. P. Waite, S. C.
503   Moran, and T. D. Mikesell (2015), Source mechanism of small long-period events at
504   Mount St. Helens in July 2005 using template matching, phase-weighted stacking, and
505   full-waveform inversion, *J. Geophys. Res.*, *120*(9), 6351-6364,
506   doi:10.1002/2015jb012279.
507 Menke, W. (1989), *Geophysical Data Analysis: Discrete Inverse Theory*, Academic Press, San
508   Diego.
509 Ohminato, T., and B. A. Chouet (1997), A free-surface boundary condition for including 3D
510   topography in the finite-difference method, *Bull. Seism. Soc. Am.*, *87*(2), 494-515.
511 Ohminato, T., B. A. Chouet, P. Dawson, and S. Kedar (1998), Waveform inversion of very long
512   period impulsive signals associated with magmatic injection beneath Kilauea Volcano, *J.*
513   *Geophys. Res.*, *103*(B10), 23,839-823,862, doi:10.1029/98JB01122.
514 Rogers, P. W. (1968), The response of the horizontal pendulum seismometer to Rayleigh and
515   Love waves, tilt, and free oscillations of the Earth, *Bull. Seism. Soc. Am.*, *58*(5), 1384-
516   1406.
517 Schimmel, M., and H. Paulssen (1997), Noise reduction and detection of weak, coherent signals
518   through phase-weighted stacks, *Geophys. J. Int.*, *130*, 497-505, doi:10.1111/j.1365-
519   246X.1997.tb05664.x.
520 Tape, W., and C. Tape (2012), A geometric setting for moment tensors, *Geophys. J. Int.*, *190*,
521   476-498, doi:10.1111/j.1365-246X.2012.05491.x.
522 Waite, G. P. (2015), Very-Long-Period Seismicity at Active Volcanoes: Source Mechanisms, in
523   *Encyclopedia of Earthquake Engineering*, edited by M. Beer, I. A. Kougioumtzoglou, E.
524   Patelli and S.-K. Au, pp. 3861-3871, Springer, Berlin, Heidelberg, doi:10.1007/978-3-
525   642-35344-4.
526 Waite, G. P., B. A. Chouet, and P. B. Dawson (2008), Eruption dynamics at Mount St. Helens
527   imaged from broadband seismic waveforms: Interaction of the shallow magmatic and
528   hydrothermal systems, *J. Geophys. Res.*, *113*(B2), B02305, doi:10.1029/2007jb005259.
529 Waite, G. P., J. J. Lyons, and P. A. Nadeau (2013), Variability in eruption style and associated
530   very-long-period earthquakes at Fuego volcano, Guatemala, *J. Geophys. Res.*, *118*(4),
531   1526-1533, doi:10.1002/jgrb.50075.
532 Wang, Z., and F. A. Dahlen (1995), Spherical-spline parameterization of three-dimensional Earth
533   models, *Geophys. Res. Lett.*, *22*(22), 3099-3102, doi:10.1029/95GL03080.
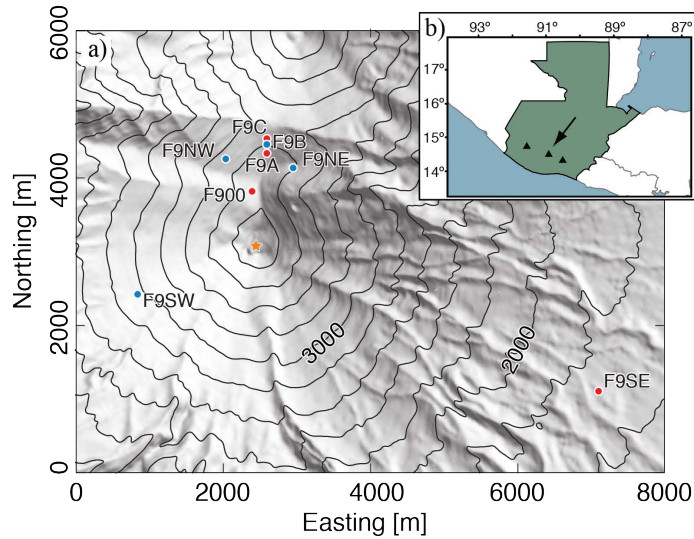534
535
536
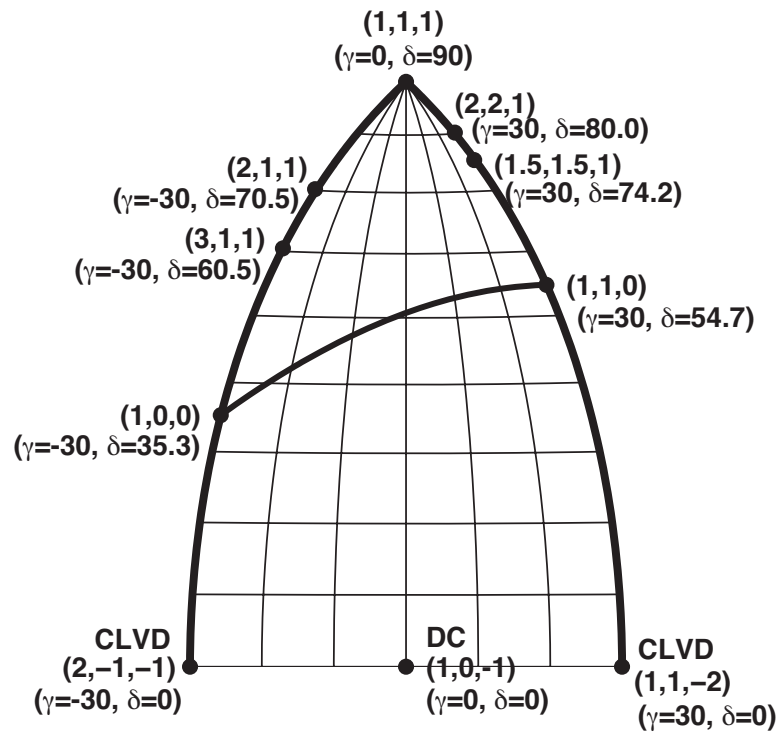
537
538   Figure 1. Example angles and corresponding moment-tensor eigenvalues are shown for common

539   source types (see Table 1) on the fundamental lune of *Tape and Tape* [2012]. All eigenvalues are

540   greater than 0 above the arc between (1,0,0) and (1,1,0). The lower hemisphere represents

541   sources with negative volume change and is not shown.

542

543

544

545   Figure 2. Locations of stations used in this study (circles) plotted on a shaded relief map of

546   Fuego volcano (a). Contour interval is 200 m. The red dots represent stations with 30 s sensors;

547   the blue dots represent 60 s sensors. The orange star marks the approximate location of the

548   summit vent. Part (b) shows the location of Fuego (arrow) in the chain of active Guatemalan

549   volcanoes. Station F9SE was not used in the inversions because the VLP signal was not observed

550   at that distance from the source.

551

552
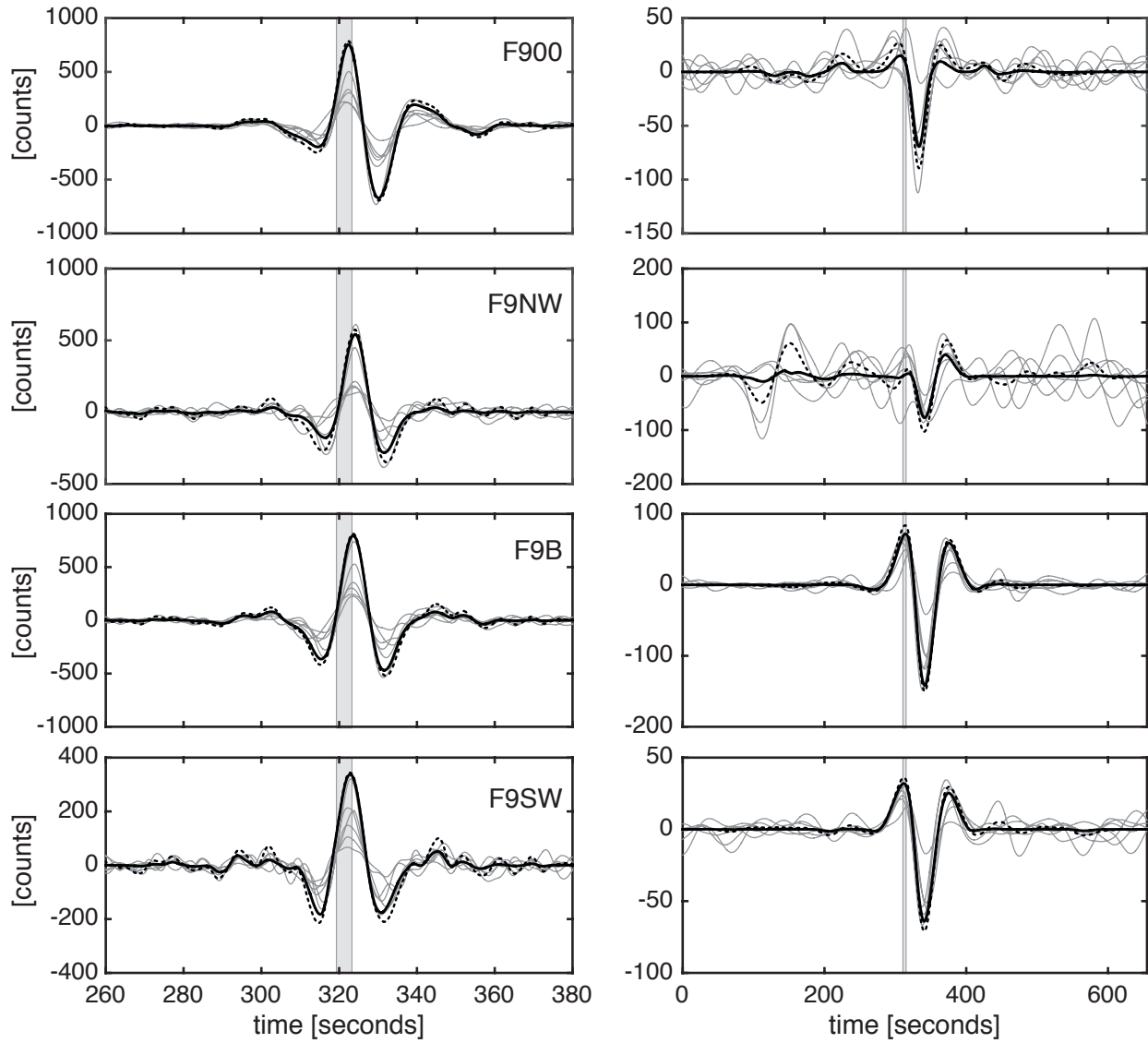
553
554 Figure 3. Bandpass-filtered (30-10 s left; 400-60 s right) seismograms from the vertical

555 component of four stations as labeled. The fine gray lines are from the six individual events used

556 in the stacks. Both linear time-domain (dashed lines) and phase-weighted stacks (bold lines) are

557 shown. Note that traces were scaled to the maximum vertical amplitude on station F900 before

558 stacking, but unscaled individual event traces are plotted. Stations F9NW, F9B, and F9SW were

559 equipped with 60 s sensors, while F900 had a 30 s sensor.

560

561

562

563

564

565

566

567

568

569

570

571

572

573

574

575

576

577
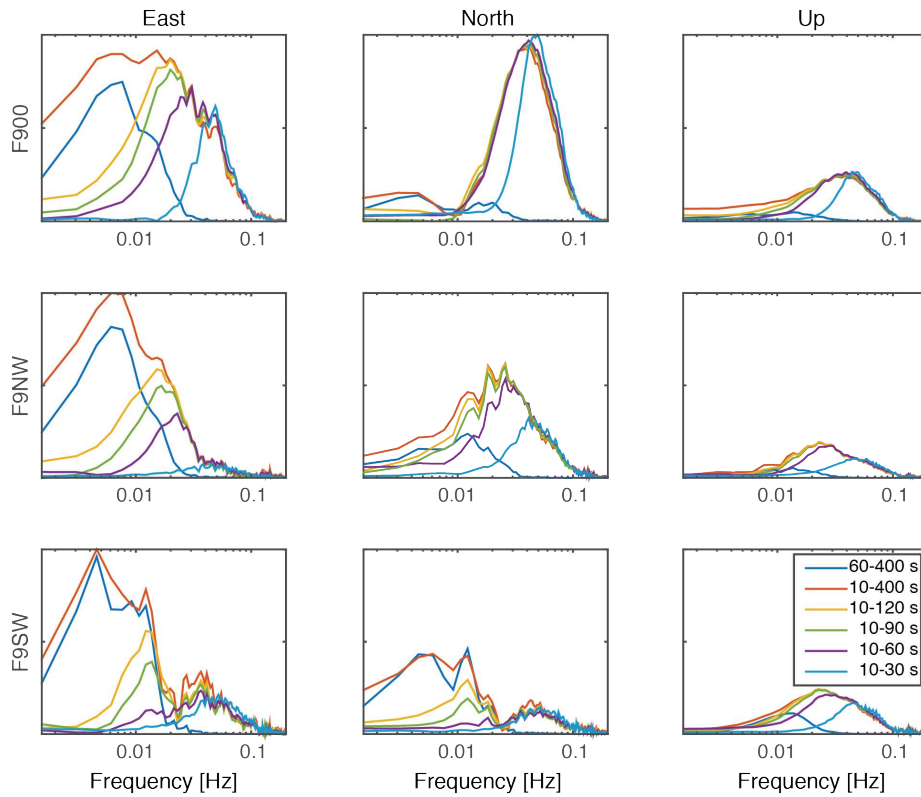
578

579

580

581

582

583

584

Figure 4. Spectra from phase-weighted stacks of bandpass-filtered seismograms from three stations as labeled. These spectra highlight the significance of the low-frequency (below the instrument corner) signal, particularly on the horizontal channels. Stations F9NW and F9SW were equipped with 60 s sensors, while F900 had a 30 s sensor. Differences between the lowest frequencies in the 400-60 s and 400-10 s stacks result from the fall off of the 2-pole Butterworth filters.
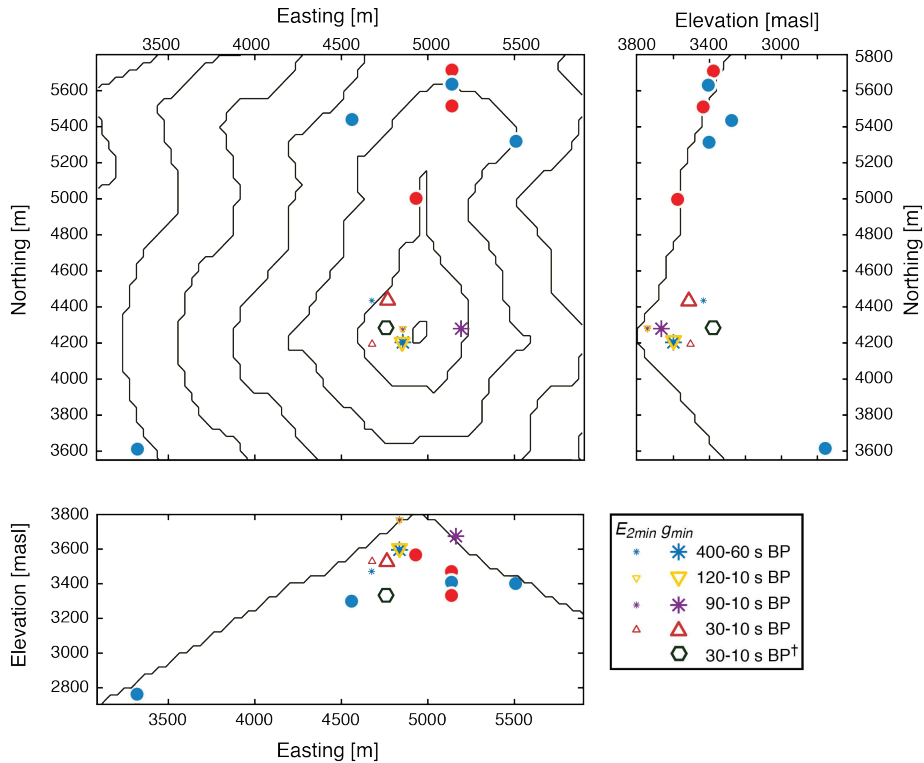
591

592

Figure 5. Locations of best-fit source centroids cluster near the summit. Both E_{2min} and g_{min} solutions are plotted by bandpass. Uncertainties on centroid locations, not shown for simplicity, are 200-350 m for solutions within 5% of the minimum. Contour interval is 200 m; the topography model plotted in map view and in the cross sections is the same as that used to compute the Green's functions. Seismic stations are shown with dots, with red dots representing stations with 30 s sensors; blue dots represent 60 s sensors as in Figure 2. The hexagon shows the best-fit location from *Lyons and Waite* [2011].

628

629

630

631

632

633

634

635

636

637

638

639

640
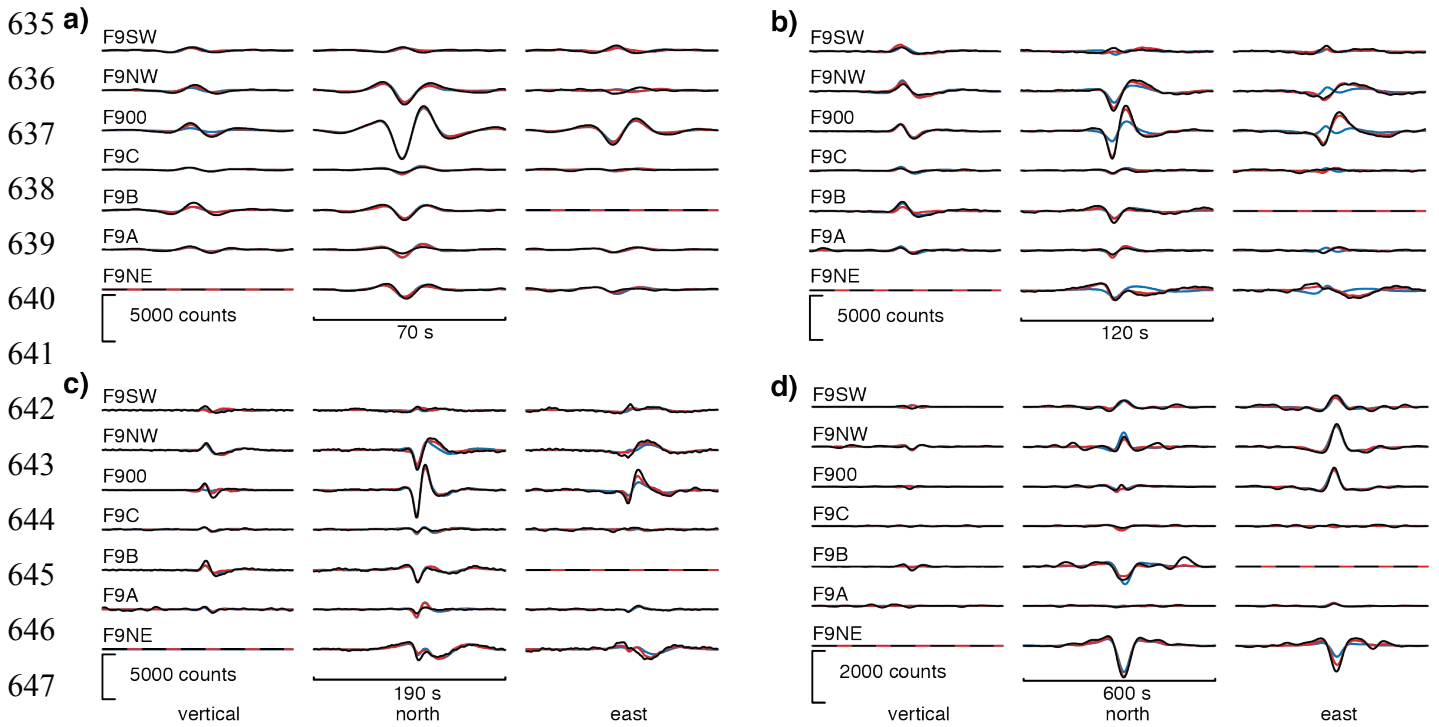
641

642

643

644

645

646

647

648

649

650

651   Figure 6. Data (black), free-inversion synthetics (red), and best-fitting constrained inversion

652   synthetics (blue) for each of the four bandpasses: a) 30-10 s; b) 90-10 s; c) 120-10 s; and d) 400-

653   60 s. The free-inversion results are generally better than the constrained inversion, as expected,

654   but this is especially true for the 90-10 s band.

655

656

657

658

659

660

661

662

663

664

665

666

667

668

669

670

671

672
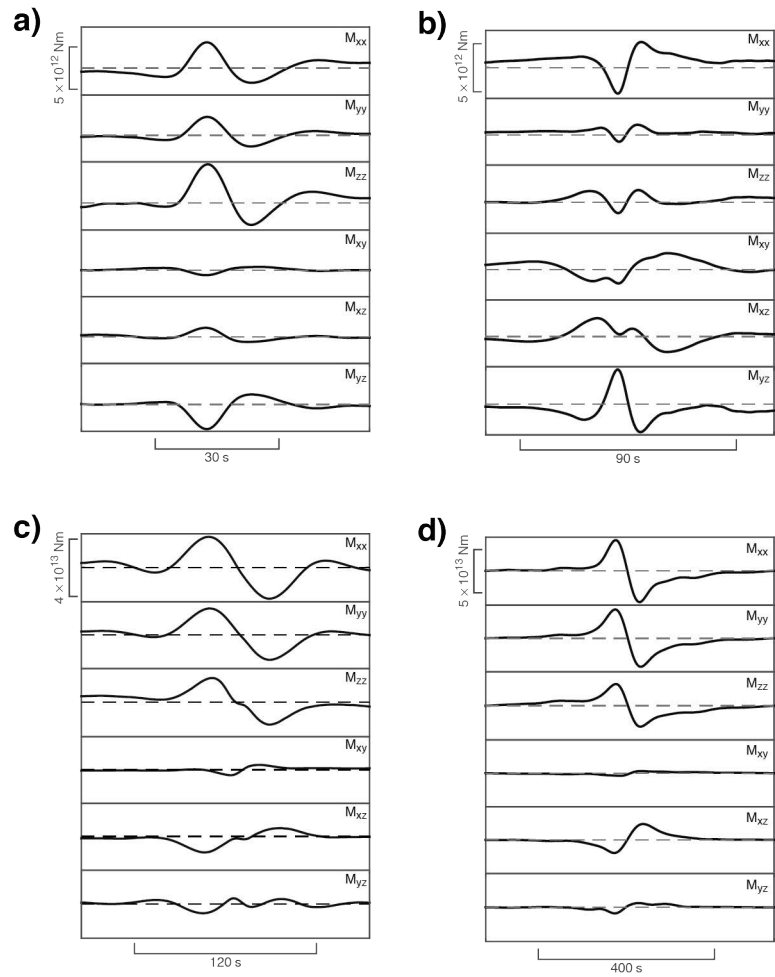
673

674

675

676

677

678

679

680

681 Figure 7. Source time functions from free inversions in the a) 30-10, b) 90-10, c) 120-10, and d)

682 400-60 s pass bands are largely consistent, although the 90-10 s band has notable differences.

683 Note the difference in amplitude and time scales for each of the four plots.

684

685
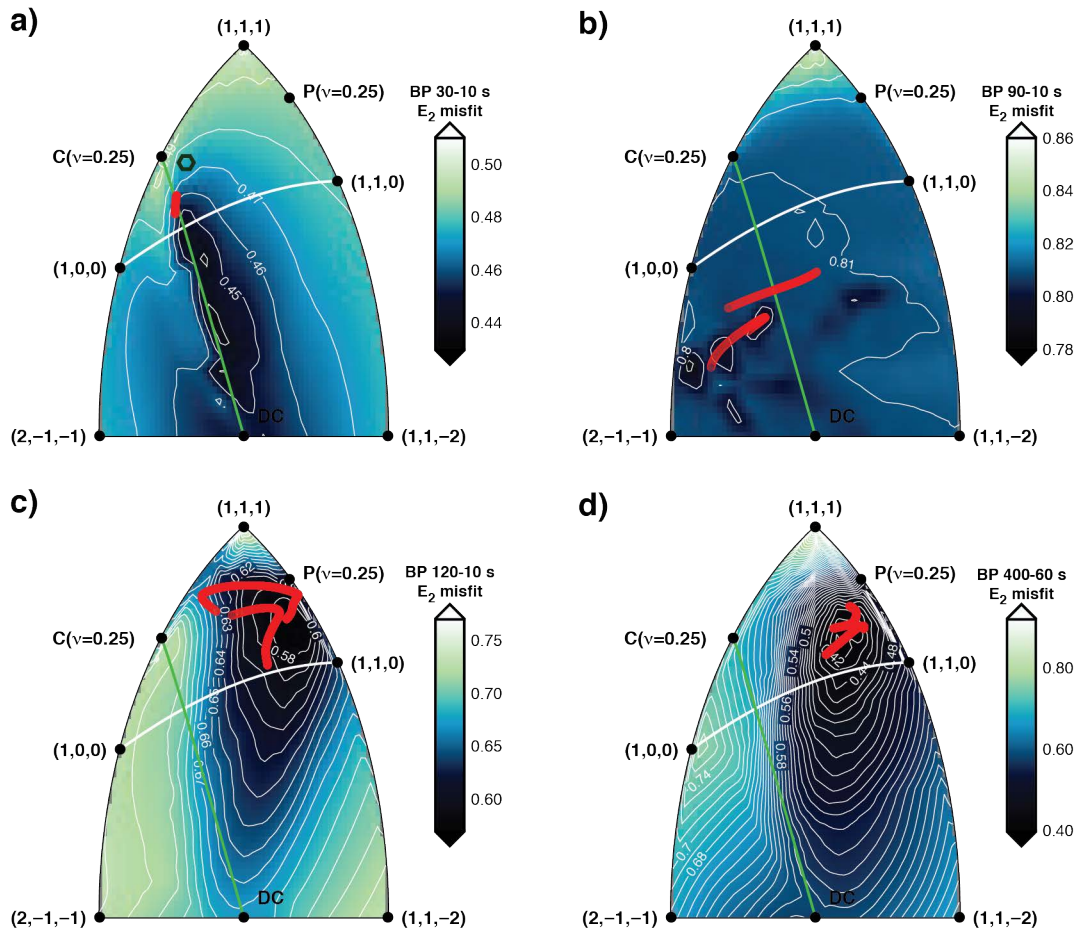
Figure 8. Error (E_2) by fixed moment-tensor solution plotted using the indicated color scale for each of the bandpasses in Figure 7: a) 30-10, b) 90-10, c) 120-10, and d) 400-60 s. The γ−δ pairs computed from the point-by-point eigenvalue analysis for the best free inversion for each of four bandpasses are plotted in red. The lack of consistency in the free inversion for the 90-10 s band is reflected in the lack of a resolved moment-tensor type. The letters C and P indicate crack and pipe, respectively. The combined crack-pipe tensor of *Lyons and Waite* [2011] is plotted as a hexagon.

Nonlinear inversion of tilt-affected very-long-period records of explosive eruptions at Fuego volcano

Gregory P. Waite[1] and Federica Lanza[1]

[1]Department of Geological and Mining Engineering and Sciences, Michigan Technological University, Houghton MI 49931 USA.

Contents of this file

Introduction

These supplementary tables include the scaled correlation coefficients and associated lag times for each data channel with the corresponding model synthetics. These tables can be compared with the waveform plots in Figure 6. Although this information is not used in the inversion, it provides additional information about the model fit that may be compared to other waveform similarity studies. Note that the correlations are scaled so that absolute amplitude information is not preserved.

band	channel	corr. coef.	lag [s]	channel	corr. coef.	lag [s]	channel	corr. coef.	lag [s]
BP 30-10 s	F9SW HHZ	0.81	0.38	F9SW HHN	0.62	-1.42	F9SW HHE	0.74	-1.64
	F9NW HHZ	0.92	0.84	F9NW HHN	0.96	-0.08	F9NW HHE	0.53	-6.50
	F900 HHZ	0.98	-0.04	F900 HHN	0.99	-0.02	F900 HHE	0.97	0.28
	F9C HHZ	0.76	-0.08	F9C HHN	0.77	-0.24	F9C HHE	0.14	-1.48
	F9B HHZ	0.96	-0.16	F9B HHN	0.91	0.00	F9B HHE	--	--
	F9A HHZ	0.60	-0.16	F9A HHN	0.83	0.02	F9A HHE	0.71	-1.20
	F9NE HHZ	--	--	F9NE HHN	0.95	0.70	F9NE HHE	0.56	-0.54
BP 90-10 s	F9SW HHZ	0.92	0.36	F9SW HHN	0.45	-0.68	F9SW HHE	0.81	0.86
	F9NW HHZ	0.93	0.34	F9NW HHN	0.95	0.22	F9NW HHE	0.91	-0.18
	F900 HHZ	0.96	-0.20	F900 HHN	0.99	0.04	F900 HHE	0.97	-0.24
	F9C HHZ	0.68	-0.64	F9C HHN	0.50	-0.16	F9C HHE	0.22	-9.98
	F9B HHZ	0.82	-0.28	F9B HHN	0.90	-0.04	F9B HHE	--	--
	F9A HHZ	0.51	-0.22	F9A HHN	0.76	0.12	F9A HHE	0.75	0.82
	F9NE HHZ	--	--	F9NE HHN	0.92	0.48	F9NE HHE	0.90	-0.68
BP 120-10 s	F9SW HHZ	0.09	9.98	F9SW HHN	0.64	-4.00	F9SW HHE	0.84	-0.70
	F9NW HHZ	0.92	0.00	F9NW HHN	0.94	0.64	F9NW HHE	0.92	0.50
	F900 HHZ	0.67	-0.42	F900 HHN	0.99	-0.12	F900 HHE	0.94	0.00
	F9C HHZ	0.68	0.72	F9C HHN	0.65	-0.22	F9C HHE	0.25	0.34
	F9B HHZ	0.92	0.88	F9B HHN	0.86	-0.08	F9B HHE	--	--
	F9A HHZ	0.46	-0.74	F9A HHN	0.71	0.60	F9A HHE	0.81	-0.22
	F9NE HHZ	--	--	F9NE HHN	0.88	-0.12	F9NE HHE	0.86	-0.94
BP 400-60 s	F9SW HHZ	-0.15	9.98	F9SW HHN	0.87	2.22	F9SW HHE	0.97	0.40
	F9NW HHZ	0.69	-0.42	F9NW HHN	0.78	0.16	F9NW HHE	0.99	1.64
	F900 HHZ	-0.08	-9.98	F900 HHN	0.78	-2.28	F900 HHE	0.98	0.62
	F9C HHZ	0.53	4.42	F9C HHN	0.77	4.54	F9C HHE	-0.26	9.98
	F9B HHZ	0.71	5.26	F9B HHN	0.89	-1.08	F9B HHE	--	--
	F9A HHZ	-0.18	9.98	F9A HHN	0.47	0.36	F9A HHE	0.86	2.88
	F9NE HHZ	--	--	F9NE HHN	0.99	-0.04	F9NE HHE	0.98	-1.98

Table S1. The correlations between each data channel and synthetic waveform from the free-inversion models, and corresponding lag times, for each channel used. The maximum allowable lag time of +/- 9.98 seconds was reached in some cases. These statistics were not computed for two channels that were not used in the inversions.

band	channel	corr. coef.	lag [s]	channel	corr. coef.	lag [s]	channel	corr. coef.	lag [s]
BP 30-10 s	F9SW HHZ	0.91	-0.78	F9SW HHN	0.73	-1.78	F9SW HHE	0.76	-0.28
	F9NW HHZ	0.92	1.58	F9NW HHN	0.94	-0.12	F9NW HHE	0.48	7.86
	F900 HHZ	0.98	-0.08	F900 HHN	0.99	-0.02	F900 HHE	0.96	0.02
	F9C HHZ	0.76	0.10	F9C HHN	0.77	0.10	F9C HHE	0.12	-0.88
	F9B HHZ	0.97	0.28	F9B HHN	0.90	0.12	F9B HHE	--	--
	F9A HHZ	0.57	-0.20	F9A HHN	0.82	0.16	F9A HHE	0.71	-0.90
	F9NE HHZ	--	--	F9NE HHN	0.95	0.86	F9NE HHE	0.48	-1.16
BP 90-10 s	F9SW HHZ	0.92	-1.64	F9SW HHN	0.24	-9.98	F9SW HHE	0.73	-1.74
	F9NW HHZ	0.94	0.32	F9NW HHN	0.93	0.02	F9NW HHE	0.54	5.58
	F900 HHZ	0.97	-0.16	F900 HHN	0.96	-0.08	F900 HHE	0.53	7.54
	F9C HHZ	0.68	-0.46	F9C HHN	0.51	-0.70	F9C HHE	0.19	-7.52
	F9B HHZ	0.97	-0.42	F9B HHN	0.79	-0.08	F9B HHE	--	--
	F9A HHZ	0.47	-0.60	F9A HHN	0.69	0.06	F9A HHE	0.46	8.18
	F9NE HHZ	--	--	F9NE HHN	0.21	1.02	F9NE HHE	-0.11	-9.98
BP 120-10 s	F9SW HHZ	0.55	3.62	F9SW HHN	0.54	-0.40	F9SW HHE	0.73	-3.94
	F9NW HHZ	0.91	1.00	F9NW HHN	0.82	0.80	F9NW HHE	0.86	-1.46
	F900 HHZ	0.80	3.56	F900 HHN	0.99	-0.10	F900 HHE	0.96	-0.52
	F9C HHZ	0.65	-0.32	F9C HHN	0.66	-0.06	F9C HHE	-0.01	9.98
	F9B HHZ	0.96	0.68	F9B HHN	0.83	0.26	F9B HHE	--	--
	F9A HHZ	0.47	0.58	F9A HHN	0.69	0.38	F9A HHE	0.77	-1.12
	F9NE HHZ	--	--	F9NE HHN	0.88	0.22	F9NE HHE	0.77	-5.20
BP 400-60 s	F9SW HHZ	-0.57	-9.98	F9SW HHN	0.85	-2.34	F9SW HHE	0.89	-4.28
	F9NW HHZ	0.66	1.26	F9NW HHN	0.75	3.08	F9NW HHE	0.98	2.56
	F900 HHZ	-0.42	-9.98	F900 HHN	0.60	-3.32	F900 HHE	0.98	2.30
	F9C HHZ	0.55	1.42	F9C HHN	0.78	1.52	F9C HHE	0.30	9.98
	F9B HHZ	0.98	-0.20	F9B HHN	0.82	-4.70	F9B HHE	--	--
	F9A HHZ	-0.23	9.98	F9A HHN	0.52	5.76	F9A HHE	0.82	3.66
	F9NE HHZ	--	--	F9NE HHN	0.99	-0.28	F9NE HHE	0.96	-2.10

Table S2. The correlations between each data channel and synthetic waveform from the fixed-inversion models, and corresponding lag times, for each channel used. The maximum allowable lag time of +/- 9.98 seconds was reached in some cases. These statistics were not computed for two channels that were not used in the inversions.